Ag nanoparticle/ZnO nanorods nanocomposites derived by a seed-mediated method and their photocatalytic properties

Xingtian Yin, Wenxiu Que[*], Duan Fei, Fengyu Shen, Qiushi Guo

Electronic Materials Research Laboratory, School of Electronic and Information Engineering, Xi'an Jiaotong University, Xi'an 710049, Shaanxi, People's Republic of China

ABSTRACT

Ag nanoparticle/ZnO nanorods (Ag NP/ZnO NRs) nanocomposites with a core/shell structure were prepared by a seed-mediated method, which contains a polyol synthesis of Ag NPs and an overgrowth process of ZnO NRs on the surface of Ag NPs. Compared with the previously reported Ag/ZnO nanocomposites which were mostly constructed by a ZnO core and a Ag shell, the nanocomposites reported in this article showed a novel structure that contained a Ag NP core and ZnO NRs shell, resulting a hedgehog-like morphology. Electron microscope images reveal that the volume content ratio of Ag NPs colloids and the ZnO precursory solution is crucial for the morphology of the resulted samples and a well-constructed Ag NP/ZnO NRs core/shell nanocomposite can be easily obtained when their volume content ratio is set at a proper value. X-ray diffraction analysis shows a good crystalline property of both Ag NPs and ZnO NRs. The relationship between the growing temperature and the morphology of the resulted samples was investigated and a possible growing mechanism of the Ag NP/ZnO NRs nanocomposites was also proposed and discussed. Furthermore, photocatalytic activities of the resulting samples with different morphologies were also studied.

© 2012 Elsevier B.V. All rights reserved.

1. Introduction

During the past decades, the synthesis of nanocomposite materials has gained a significant attraction and a lot of efforts have been made to prepare materials with different compositions and morphologies. For example, ZnO/V_2O_5 core/shell nanostructures [1], ZnO/TiO_2 nanocomposites arrays [2], ZnTe/ZnO branched nanoheterostructures [3], and ZnO/Cu_2O composite crystals [4] have been synthesized and enhanced photocatalytic properties have been observed. Among all the nanocomposite materials, metal-semiconductor heterogeneous nanocomposite materials have been attracting extensive scientific and technological interest due to their unique optical, electrical, and catalytic properties which may be of great use in developing future nanoscale optoelectronic devices. For example, the Fermi level of Au/TiO_2 composite can be shifted to more negative potential due to the charge equilibration of the composite system when the semiconductor and metal are in contact, and the shift in the apparent Fermi level of the composite can be adjusted by the size of the Au nanoparticles [5]. Metals such as Au and Ag possess electron storage properties which in turn facilitate to improve charge separation in semiconductor-metal composite systems [6]. These properties have been investigated in the fields of biomedicine [7],

nanodevices [8] and photoluminescence [9,10]. Particularly, photocatalysts based on semiconductor-metal composite materials have been studied in detail [11–19].

Compared with all other metal-semiconductor heterostructures, Ag/ZnO nanocomposites have drawn particular attention, not only because ZnO with different nanostructures can be easily prepared by a series of simple methods [20–23], but also that silver displays the most efficient plasmon resonance in the visible region among all metals by virtue of its favorable frequency dependence of the real and imaginary parts of the dielectric function [24]. For example, enhanced Raman scattering has been attained by using a Ag nanocluster/ZnO nanowire array as the surface-enhanced Raman scattering substrate [25,26]. It has been reported that Ag/ZnO composite system exhibits enhanced photocatalytic property compared with the pure ZnO, which mainly results from the inhibited recombination of the photoinduced electrons and holes by the heterostructures [15,16]. Thus, Ag/ZnO nanocomposites with different structures and morphologies have been prepared by different methods, such as Ag/tetrapod-like ZnO whisker nanocompounds [15], Ag nanoparticles/ZnO nanorods (Ag NPs/ZnO NRs) [16], Ag/ZnO nanofibers [17], Ag nanoparticles-stabilized ZnO nanosheets [27]. Besides, Ag NPs/ZnO NRs arrays have also been synthesized by electrodeposition and photocatalytic method [28,29]. Apart from all these Ag/ZnO nanocomposites, ZnO/Ag core/shell nanostructures have been derived from varies routes and their extraordinary properties have been investigated in detail [30,31]. Besides, Ag/ZnO core/shell Nanoparticles in which
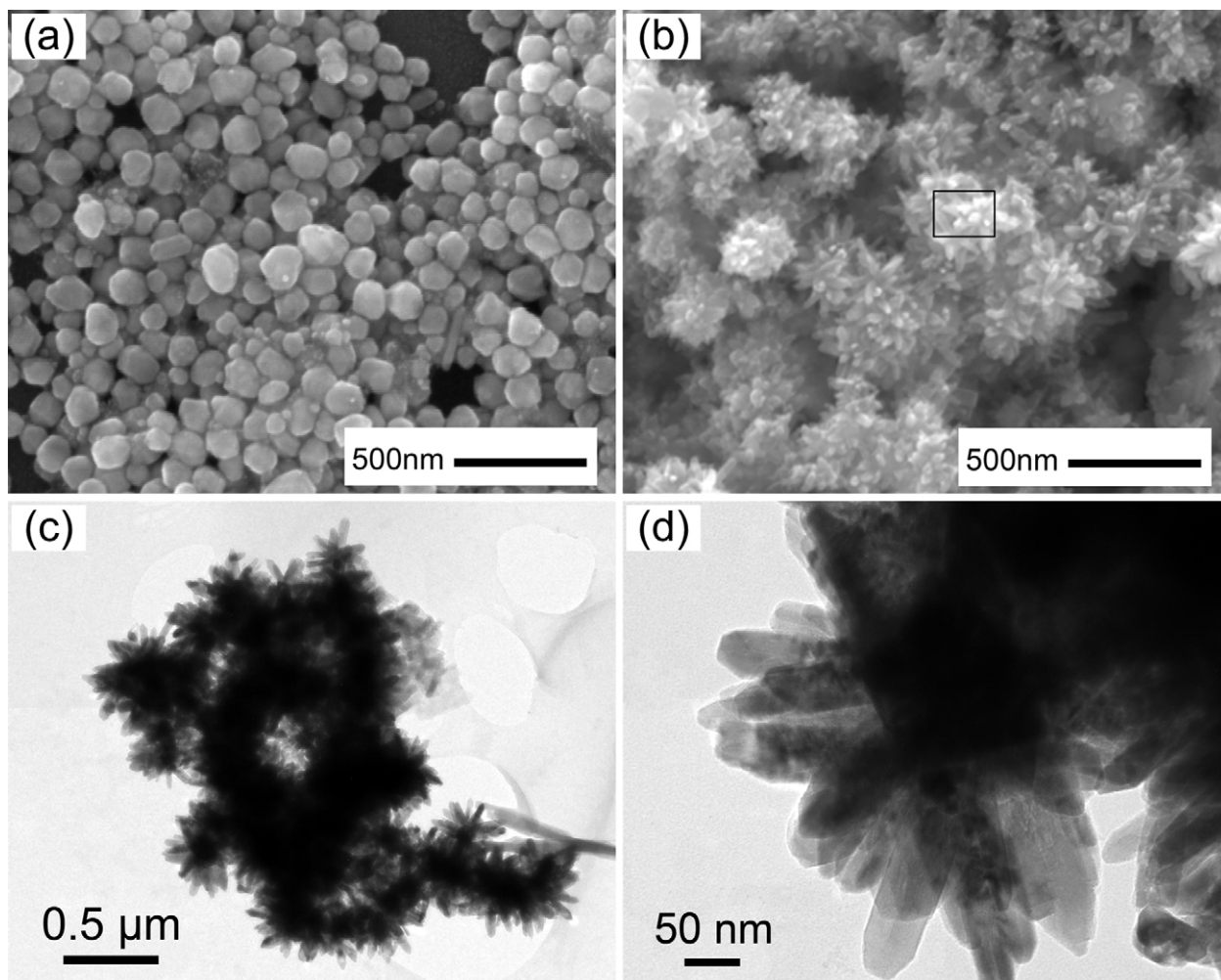
Fig. 1. (a) FE-SEM image of the Ag particles; (b) FE-SEM image, (c) low-magnified TEM image, (d) high-magnified image of the Ag NP/ZnO NRs core/shell nanocomposites from 8 mL precursory solution (S3).

Ag NP acts as the core and ZnO acts as the shell have also been successfully prepared by Aguirre et al. [32]. However, works on nanocrystals constructed by Ag cores and ZnO shells are still limited.

Here, we report a seed-mediated method to prepare Ag NP/ZnO NRs nanocomposites with a core/shell structure, which contains a polyol synthesis of Ag NPs and an overgrowth process of ZnO NRs on the surface of the Ag NPs. Results indicate that the morphology and composition of the resulted samples depend on the volume content ratio of the Ag NPs colloids and the ZnO precursory solution in the overgrowth process of the ZnO NRs, and a perfect Ag NP/ZnO NRs core/shell nanocomposite with good crystalline property can be obtained by optimizing the value of this ratio. It is also shown that a higher growth temperature leads to shorter and wider nanorods of the shell on the Ag core. A possible growing mechanism of the Ag NP/ZnO NRs nanocomposites was proposed. In addition, photocatalytic properties of the resulted samples were also measured and discussed. Unlike the enhanced photocatalytic performance of Ag/ZnO composite nanocrystals reported in other literatures which mainly resulted from the inhibited recombination of the photoinduced electrons and holes due to the formed heterostructure [15,16], the enhanced photocatalytic activities shown in our experiment should be ascribed to both the heterostructure and the smaller size of resulted crystals due to the introduction of Ag seeds in the ZnO precursory.

2. Experimental details

2.1. Materials

All the chemicals were used as received without any further purification. Silver nitrate was purchased from Shanghai Chemical Reagent Co. Ltd. China and the rest chemicals were purchased from Sinopharm Group Chemical Reagent Co. Ltd. China. Deionized water with a resistivity of 18.3 MΩ cm was used in all the preparation.

2.2. Preparation of Ag NPs

Ag NPs were prepared by a traditional polyol synthesis process with a little modification [33], in which ethylene glycol (EG) serves as both solvent and reducing agent. In a typical procedure, 5 mL of EG was added into a 50 mL round-bottom flask and heated to 160 °C in an oil bath. Then, 3 mL of polyvinyl pyrrolidone (PVP) solution (0.375 M in EG) was injected into the flask with stirring. Two minutes later, 3 mL of AgNO$_3$ solution (0.25 M in EG) was also injected into the hot solution drop by drop under vigorous stirring. The mixture was then stirred at the temperature for another 40 min before cooling down to room temperature in cold water. Thus, the obtained colloid without any other disposal was employed as a seed solution for further growth of ZnO NRs on the surface of Ag NPs, and a small portion of the colloid was centrifuged at 10,000 rpm for 8 min and washed twice with ethanol, then dispersed in ethanol for characterization.

2.3. Synthesis of Ag NP/ZnO NRs nanocomposites

To grow ZnO NRs on the surface of Ag NPs, a precursor solution which contains 0.04 M Zn(NO$_3$)$_2$ and 0.8 M NaOH was firstly prepared. Then, 2 mL seed colloids was injected into a Teflon-lined stainless steel autoclave of 30 mL capacity, followed by an addition of different amounts of water and the precursory solution under a

vigorous stirring, and the total volume of the reaction solution was fixed to 24 mL. The autoclave was sealed and heated to different temperature in a furnace for 1 h. It was then allowed to cool naturally to room temperature. The product was centrifuged at 6000 rpm for 10 min and washed twice with ethanol, then dried at 80 °C for further characterization.

2.4. Characterization

X-ray diffraction (XRD) analysis was employed to characterize the crystalline properties of the resultant Ag/ZnO nanocomposites, using a D/max 2400 X Series X-ray diffractometer. The X-ray radiation source used was Cu Kα, obtained at 40 kV, 100 mA and the scanning speed was 10° min^{-1} at a step of 0.02°. Transmission electron microscopy (TEM) (JEM-2100F, JEOL Inc., Japan) and a field emission scanning electron microscopy (FE-SEM) equipped with a energy dispersive X-ray detector (EDX) (JSM-6700F, JEOL Inc., Japan) were used to characterize the morphology and composition of the Ag/ZnO nanoparticles. The UV–vis absorption spectra were measured by a V-570 UV–visible (UV–vis) spectrophotometer from Jasco Corp. X-ray photoelectron spectroscopy (XPS) was used to analyze elemental and chemical states of the silver in the composite, using Al Ka radiation as the X-ray source (ESCALAB MK-II model), operated at 12.5 kV and 20 mA under a vacuum pressure of 10^{-8} Pa. Surface Area and Property Analyzer (ASAP-2020, MICROMERITICS, USA) was employed to measure the Brunauer–Emmett–Teller (BET) specific surface areas of the resulted samples. Photoluminescence (PL) spectra were performed at room temperature using a He:Cd laser with a wavelength of 325 nm.

2.5. Photocatalytic measurement

Photocatalytic activities of the samples were also measured by using methyl orange (MO) as a representative dye indicator. 30 mg of each sample was suspended in 100 mL of a standard MO aqueous solution (20 mg/L) and magnetically stirred in dark for 1 h to attain equilibrium adsorption on the sample surface. The mixture was then loaded in a tube and exposed to a high-pressure mercury lamp (300 W) with continuously stirring. After a given irradiation time, a certain volume of the suspension was withdrawn and the photocatalyst was separated from the suspensions by centrifuging. The residual MO aqueous solution was measured by the UV–vis absorption spectroscopy to evaluate the photocatalytic degradation process.

3. Results and discussion

In order to simplify the statement, samples prepared with different parameters were named and listed in Table 1. Fig. 1(a) and (b) shows the representative FE-SEM images of the Ag seeds and the Ag NP/ZnO NRs nanocomposites prepared with 8 mL precursory solution (S3). In Fig. 1(a), round-like but erose Ag NPs with a diameter in the range of 50–150 nm can be clearly observed. After an overgrowth process of ZnO NRs on the surface of Ag NPs, hedgehog-like nanocomposites can be seen as shown in Fig. 1(b), indicating that ZnO NRs can grow directly on the surface of Ag NPs without any other ancillary seed-assisted process. TEM images were further taken to investigate the detailed structure of the hedgehog-like nanocomposites. Fig. 1(c) shows a low-magnified TEM image of the sample, from which well Ag NP/ZnO NRs core/shell nanocomposites can be identified. All these hedgehog-like nanocomposites tightly adhere to each other due to an interdigital connection among these ZnO NRs. A high-magnified TEM image of an individual Ag NP/ZnO NRs nanocrystal is shown in Fig. 1(d), which shows the core/shell nanocrystal is constructed by a Ag core with a diameter of about 140 nm in the center and tens of ZnO NRs with an typical length of 80–120 nm and typical diameter of 40–70 nm around the Ag NP. Fig. 2 shows the EDX spectrum of the rectangle area indicated in Fig. 1(b). Both peaks of Ag and Zn can be clearly seen, which further confirms the composition of the hedgehog-like core/shell nanocomposites.

To investigate the crystal structure of the as-prepared nanocrystals, the Ag NPs and the Ag NP/ZnO NRs nanocomposites (S3) dispersed in ethanol were dropped onto clean silicon wafers and then dried in air for XRD characterization. Fig. 3 presents their XRD patterns, which there are three peaks at 38.1°, 44.2° and 64.4° corresponding to (1 1 1), (2 0 0) and (2 2 0) planes of the Ag NPs, respectively. It should be noted that the peak of the (1 1 1) plane in intensity is much more intense than those of other two peaks, suggesting that the Ag seeds are mainly enclosed with the (1 1 1)
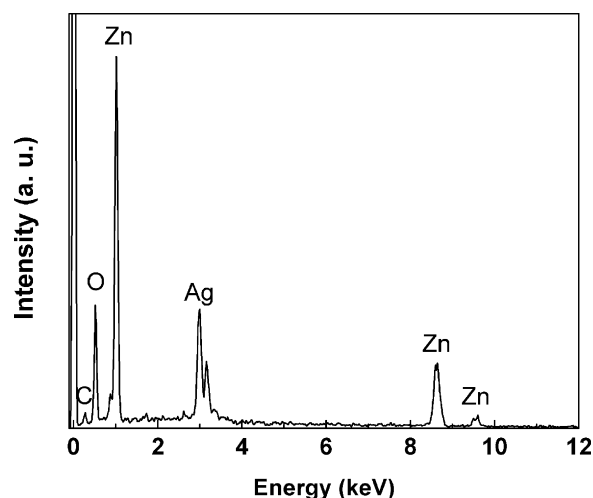

Fig. 2. EDX spectrum of the rectangle area as indicated in Fig. 1(b).

planes. In addition, two separate phases are also noted for the Sample S3, which corresponds to face-centered cubic (fcc) Ag and wurtzite ZnO, indicating a good crystalline property of the resulting sample.

To explore the mechanism of the overgrowth progress of the ZnO NRs on the surface of Ag NPs in our experiment, the volume content ratio of the Ag NPs colloids and the ZnO precursory solution was varied, with the accurate values presented in Table 1. The morphology of the resulting nanocrystals was characterized by FE-SEM. Fig. 4(a)–(f) shows the FE-SEM images of the samples from 4 mL, 6 mL, 10 mL, 12 mL, 22 mL and 24 mL precursory solution, which are named as S1, S2, S3, S4, S5, S6 and S7 as listed in Table 1, respectively. It can be seen from Fig. 4(a) that despite some nanosheets, only a few ZnO NPs locate on the surface of Ag NPs. When the volume content of the precursory solution is increased to 6 mL (S2), some larger particles assembled by a lot of small nanoparticles are observed as shown in Fig. 4(b). Comparing with the structure of the sample S3 (as shown in Fig. 1), it can be suggested that these larger particles should be composed of the Ag NP core and the ZnO NPs (or ZnO NRs) shell, which will be further proven by the TEM images as shown later. If the volume content of the precursory solution is further increased to 10 mL (S4), hedgehog-like nanoparticles that are similar to those shown in the sample S3 are obtained. The length
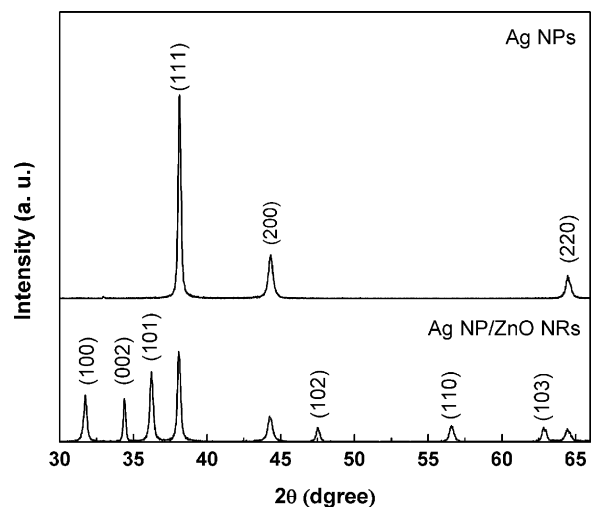

Fig. 3. XRD patterns of the Ag particles and the Ag NP/ZnO NRs nanocomposites from 8 mL precursory solution (S3).

Table 1
Detail synthesis conditions and size parameters of the resulted samples.

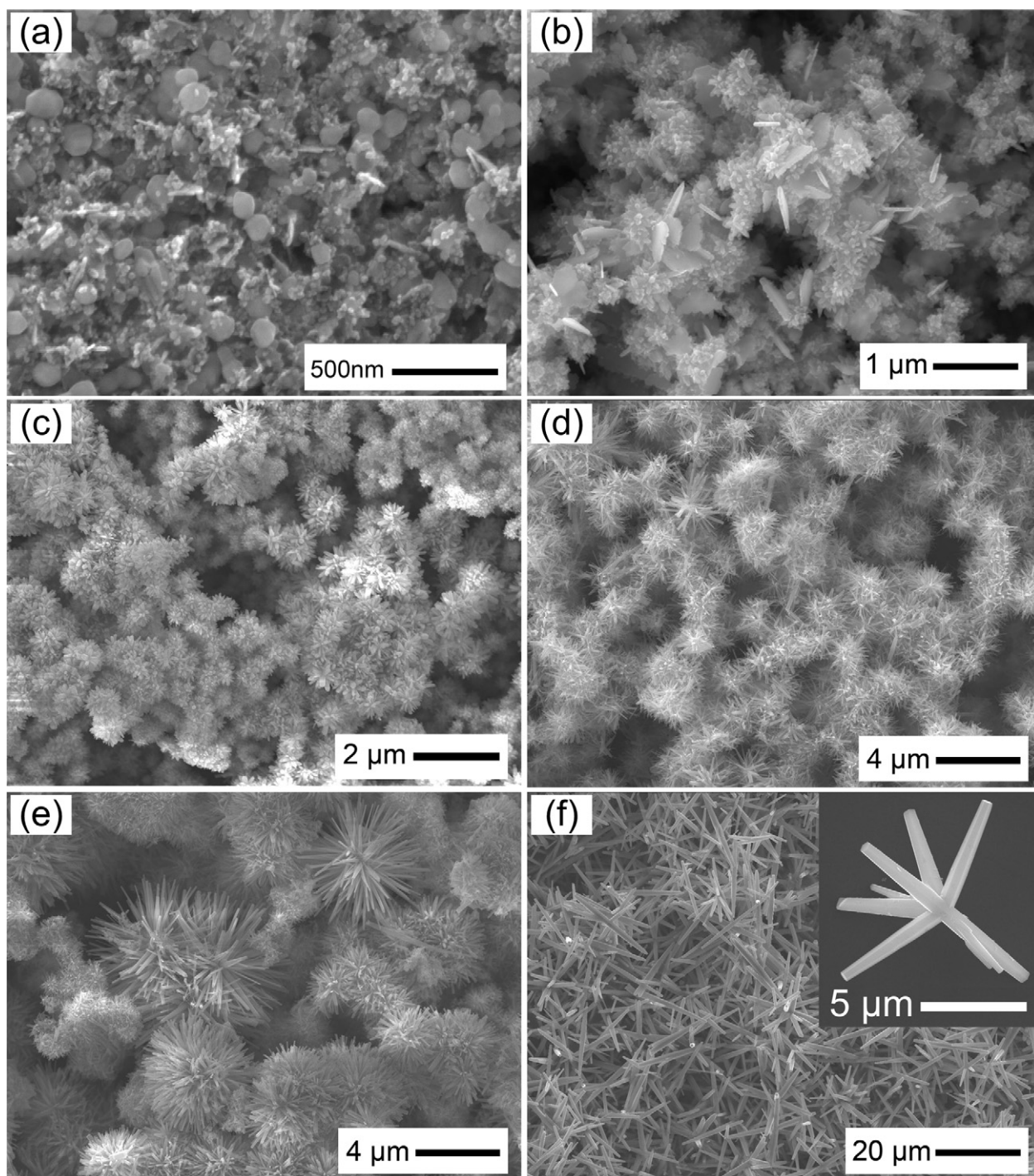| Sample	Ag NPs colloids (ml)	Precursory solution (ml)	Growth temperature (°C)	Length of the ZnO NRs (μm)	Diameter of the ZnO NRs (nm)
S1	2	4	150	~0.06	~30
S2	2	6	150	~0.07	~50
S3	2	8	150	0.08–0.12	40–70
S4	2	10	150	0.2–0.3	40–120
S5	2	12	150	0.35–1.2	50–150
S6	2	22	150	0.5–2	50–230
S7 (pure ZnO)	0	24	150	5–20	400–1500
S8	2	8	80	0.1–0.14	10–20
S9	2	8	200	0.05–0.1	20–60

Fig. 4. FE-SEM images of the samples: (a) S1, (b) S2, (c) S4, (d) S5, (e) S6 and (f) S7, respectively.
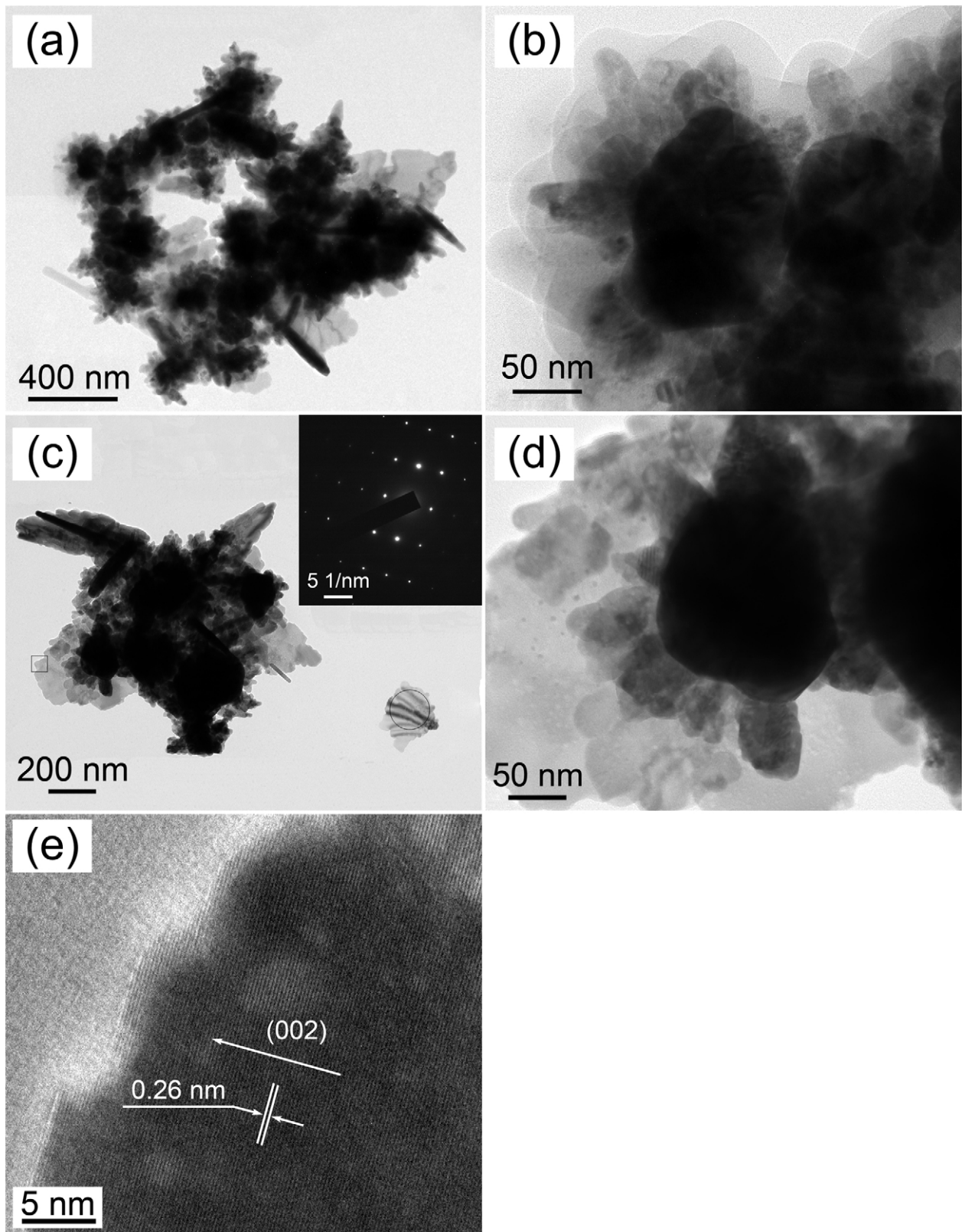
Fig. 5. (a) and (b) The low-magnified and high-magnified TEM images of the sample S1, respectively; (c) and (d) the low-magnified and high-magnified TEM images of the sample S2, respectively (the inset of c shows the electron diffraction pattern of the nanosheet noted by the circle); (d) high-resolution TEM image of the area indicated by the square in (c).

of ZnO NRs on the Ag NPs is in the range of 200–300 nm which is longer than that of the Sample S3. It should be mentioned here that for the sample S4, no any nanosheet is observed. The length of the ZnO NRs shown in Fig. 4(d) is more than 350 nm as the volume

content of the precursory solution is increased to 12 mL. Especially, as shown in Fig. 4(e), both big nanocomposite particles consisted of ZnO NRs in the length of more than 2 μm and small ones consisted of ZnO NRs in the length as short as 500 nm are observed

in the sample obtained from 22 mL precursory solution (S6). These results indicate that the length of ZnO NRs on the surface of Ag NPs increases with the volume content of the Zn source. Fig. 4(f) shows the FE-SEM image of the sample prepared without any Ag NPs colloids (S7), and the inset presents an individual ZnO crystal, in which several nanorods in the length of ca. 5 μm growing from one ZnO nuclei is observed, indicating that if no Ag NPs colloids are added into the initial reaction mixture, only large-size star-like pure ZnO nanocrystals can be grown.

In order to understand the growth process of the ZnO NRs on the surface of Ag NPs, especially at the initial period during which the ZnO nuclei forms on the surface of Ag NPs, TEM was further used to observe the structure of the samples S1 and S2. Fig. 5(a) and (b) shows the low magnified and high magnified TEM images of the sample S1, respectively. It can be clearly observed that most Ag NPs are crowded by a lot of small nanocrystals, which are believed to be ZnO NPs. It can be also seen from Fig. 5(b) that in spite of losing their rod shape due to lack of the Zn source, most ZnO nanocrystals adhere well to the surface of Ag NPs. Fig. 5(c) shows the low magnified TEM image of the sample S2, from which both Ag NP/ZnO NRs core/shell structure and the nanosheets are observed. The inset shows the electron diffraction pattern of the nanosheet noted by the circle in Fig. 5(c). Obviously, this pattern represents the diffraction of the ZnO crystal, indicating that the nanosheets shown in the samples S2 and S1 are composed of the ZnO crystal. Fig. 5(d) shows a typical individual Ag NP/ZnO NRs particle, which is very similar to that shown in the sample S1. Fig. 5(e) shows a high-resolution TEM image of the area indicated by the square as shown in Fig. 5(c). The spacing between two adjacent lattice fringes is 0.260 nm, corresponding to the (0 0 2) plane of ZnO, which further confirms that the component of the nanosheet is ZnO.

Effect of the growth temperature on the morphology of the Ag/ZnO nanocomposites was also investigated. Fig. 6(a) and (b) shows the SEM images of the samples obtained from 8 mL precursory solution at 80 °C (S8) and 200 °C (S9), respectively. The ZnO NRs shells with a typical length of 100–140 nm and a typical diameter of 10–20 nm can be clearly observed for the sample S8. It can be also seen from Fig. 6 that when the growth temperature is increased to 200 °C, the ZnO NRs become shorter and wider and some ZnO NRs even gradually lose their rod shape. As compared to the images of the sample S3 as shown in Fig. 1, it can be concluded that with an increase of the growth temperature, much more ZnO NRs with smaller length and bigger diameter can be grown on the surface of Ag NPs. One possible explanation is that higher growth temperature is beneficial for ZnO to nucleate on the Ag NPs surface, that is to say, it is easier to form plenty of ZnO nuclei at the very beginning of the overgrowth process. Thus, the adjacent nuclei may fuse together and form larger ones, resulting wider nanorods. At the same time, considering the Zn source is limited and the nuclei are excessive, so that it is difficult to obtain longer ZnO NRs under such condition.

XPS was employed to clarify the chemical state in the Ag NPs/ZnO NRs nanocomposites, and the spectra of Ag 3d and O 1s core levels are shown in Fig. 7(a) and (b), respectively. The shift of binding energy due to relative surface charging has been corrected using the C 1s level at 284.6 eV as an internal standard. There are two adjacent peaks at 367.8 eV and 373.9 eV for the sample S1 in Fig. 7(a), which correspond to Ag $3d_{5/2}$ and Ag $3d_{3/2}$, respectively, indicating a metallic nature of silver. Compared with the standard value of bulk Ag (368.2 eV), the $3d_{5/2}$ peak of Ag in our work shifts to lower binding energy due to the intense interaction between Ag and ZnO nanocrystals. However, for the sample S3, no peak of Ag is detected, indicating that all the surface of Ag NPs is covered by ZnO. In Fig. 7(b), two adjacent peaks at 530.2 eV and 531.6 eV are observed for the sample S1, corresponding to the lattice oxygen of ZnO and chemisorbed oxygen caused by the surface hydroxyl, respectively [16]. For the sample S3, the relative
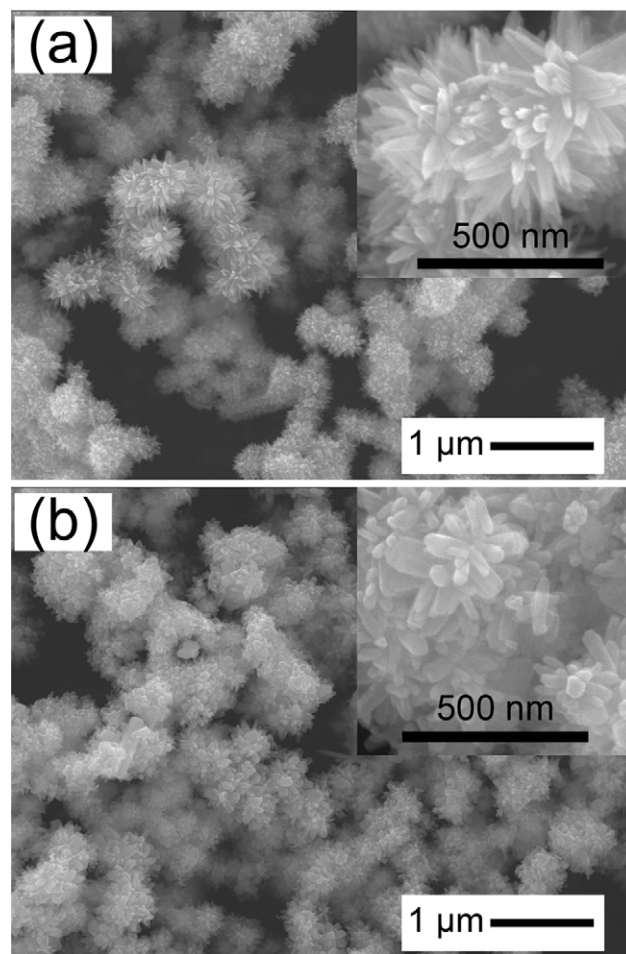

Fig. 6. FE-SEM images of the samples: (a) S8 and (b) S9, respectively.

intensity of the peak for chemisorbed oxygen decreases rapidly, because much more lattice oxygen of ZnO can be detected due to the completely coverage of ZnO on the surface of Ag NPs, and thus the relative amount of absorbed oxygen decreased a lot.

Based on the above results and discussion, the growth process of the Ag/ZnO nanocomposites can be explained as follows. Generally speaking, there are two significant periods, including nucleation and growth. For the overgrowth process of the ZnO NRs on the surface of Ag NPs, if no Ag NPs exists in the growth solution, ZnO nucleation occurs homogenously in the solution and then they will be mainly epitaxial along (0 0 2) plane due to its larger growth velocity. Since the nuclei may have several (0 0 2) planes, thus, they will be epitaxial to form star-like crystals (Fig. 4(f)). When a proper amount of Ag NPs colloids is added into the growth solution, ZnO nucleation will be easier to occur on the surface of Ag NPs. It has been reported that ZnO NRs can grow directly on the facets of Ag NPs without any other ancillary seed-assisted process, especially, ZnO NRs preferentially grow on the (1 1 1) rather than the (1 0 0) facets of truncated Ag nanocubes in aqueous solution due to the good lattice and symmetry match between ZnO and Ag in the corresponding planes [34]. Thus, the overgrowth process in our experiment can be illustrated in Fig. 8. Since the Ag seeds used in our experiment are mostly round-like particles, which are mainly enclosed with (1 1 1) plane, thus, ZnO is easy to nucleate and grow homogenously on the surface of Ag NPs. For the overgrowth process, firstly, ZnO nucleates on the surface of Ag NPs. Then, if the relative content of the Zn source is insufficient, these nuclei only grow to become bigger particles and few nonorods can be obtained
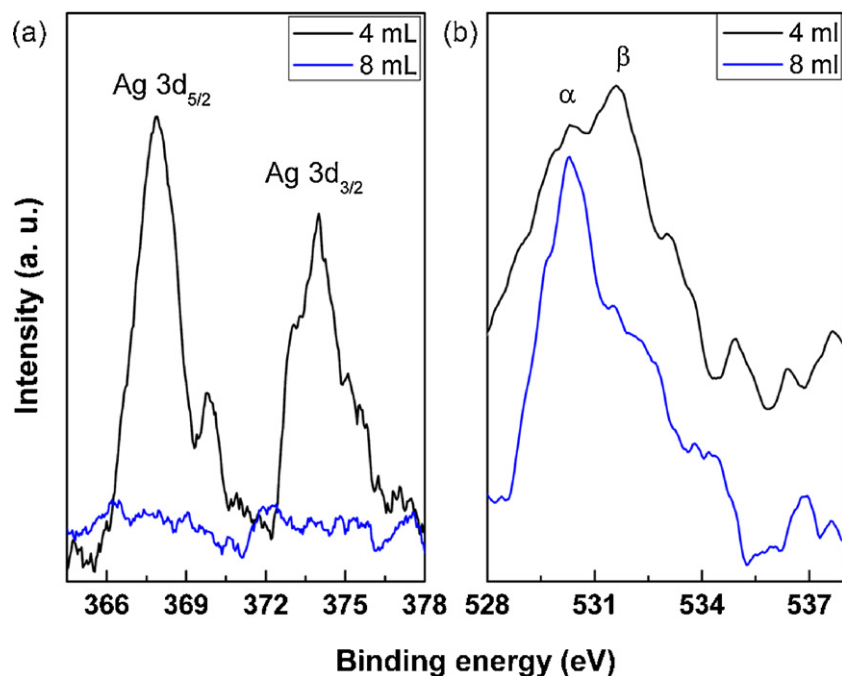
Fig. 7. XPS spectra of the Ag NP/ZnO NRs nanocomposites.

as shown in Figs. 4(a) and 5. On the contrary, if excessive Zn source is provided, the nuclei on the surface of Ag NPs will grow too long along (0 0 2) plane of ZnO to maintain their nanostructure as shown in Fig. 4(e). Therefore, only when the volume content ratio of the Ag NPs colloids and the ZnO precursory solution in the reaction mixture is optimized at a proper value, which includes 2 mL Ag seed colloid and 8 mL precursory solution in our experiment, a perfect Ag NP/ZnO NRs core/shell nanocomposite can be obtained.

Fig. 9(a) shows the UV–vis absorption spectra of the samples, which are all measured using an integrating sphere except for the Ag seeds colloids. It can be seen that there is an absorption peak centering at 420 nm for the Ag NP seeds colloids due to the surface plasmon effect of Ag NPs, and the pure ZnO shows an intense near band absorption at about 380 nm. While compared with the pure ZnO, all the Ag NP/ZnO NRs nanocomposites show more intense absorption in the visible region, and besides the near band absorption, an absorption shoulder at about 420 nm is also identified. Interestingly, the sample S3 shows the most intense absorption at 420 nm, because the samples S5 and S6 have much "thicker" ZnO layer on the surface of Ag NPs and the sample S1 contains many ZnO nanosheets as shown in Figs. 4 and 5, both of which can reduce the relative absorption intensity of Ag NPs in the composite nanocrystals. The PL spectra of the as-synthesized Ag NP/ZnO NRs nanocomposite are shown in Fig. 9(b). For the pure ZnO, a broad green emission peak centering at 553 nm is observed, which should be ascribed to the intrinsic defects of ZnO [16]. Besides, a weak peak centering at 390 nm for the near-band emission of ZnO is also observed. However, no obvious peak in the visible region is found for all the Ag NP/ZnO NRs nanocomposites, and the received photo signal intensity in the whole region is very low due to the incorporation of Ag NPs, suggesting that the Ag NPs incorporated into the nanocomposites have a quenching effect on the light emission of ZnO in the visible region.

Photocatalytic activities of some resultant samples were measured and presented in Fig. 10. It can be seen that after being irradiated under UV light for 90 min, only 20% of MO is photo-degraded for the pure MO aqueous solution, indicating that MO is stable enough for the investigation of the photocatalytic

activity of the resultant photocatalyst. It is noted that if the pure ZnO (S7) is added into the MO aqueous solution, the MO degradation rate is obviously faster than that as observed in the blank test. As a comparison, the photocatalytic activity of pure Ag NPs was also investigated, and the results showed that only 9% of MO aqueous solution is photo-degraded after being irradiated under UV light for the same time. This value is even smaller than that of pure MO aqueous solution under UV light, suggesting the non-photocatalytic property of Ag NPs towards to MO. When the sample S1 is used as the photocatalyst, about 77% MO can be photocatalytic-degraded, which is slightly higher than that of the pure ZnO (70%). As the sample S3 with a higher volume content precursor solution in the initial reaction mixture is used as the photocatalyst, the MO degradation rate become faster and more than 85% MO can be photocatalytic-degraded. It should be noted that the samples S5 and S6 show a similar photocatalytic performance and more than 93% MO can be photocatalytic-degraded within 90 min. indicating these two samples have a better photocatalytic activity for the MO degradation.

Many works have been reported on the enhanced photocatalysis of Ag/ZnO nanocomposites, and the inhibited recombination of the photoinduced electrons and holes due to the formed heterostructure was believed to be the most important reason for this enhancement [15,16]. However, the comparison of the photocatalytic performance in our experiment is much more complex due to the huge difference of size and morphology among samples. The sample S1 exhibits a better photocatalytic performance than the pure ZnO (S7), whereas the content of ZnO in the sample S1 is much fewer than that in the sample S7. Therefore, this enhancement effect is probably related to the formed heterostructure in this nanocomposite, which is believed to inhibit the recombination of the photoinduced electrons and holes effectively. The BET specific surface area measurement shows that the specific surface area increases rapidly from $0.35 \, m^2/g$ for the pure ZnO to $9.01 \, m^2/g$ for the sample S1 and $10.28 \, m^2/g$ for the sample S3. Thus the larger specific surface area of the sample S1 also contributes to its better photocatalytic performance, because it is possible to provide much more interface between the MO and the
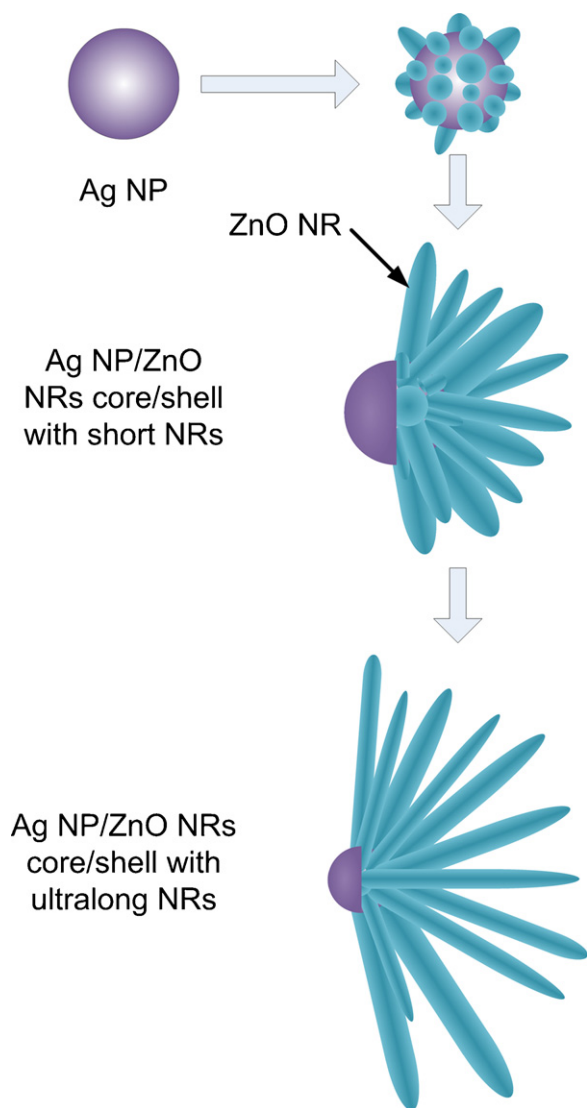
Fig. 8. Illustration of the overgrowth process of the ZnO NRs on the surface of the Ag NP.

Fig. 9. (a) UV–vis absorption spectra and (b) PL spectra of the synthesized samples.
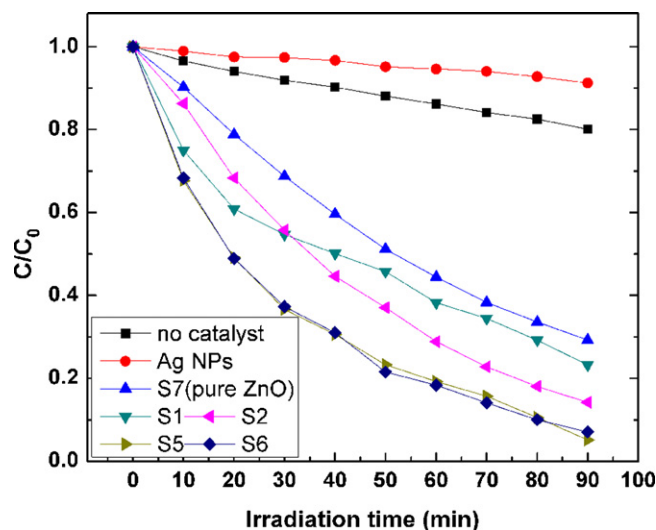
Fig. 10. Photocatalytic degradation kinetics of the MO aqueous solution of the synthesized samples.

photocatalyst which can accelerate the degradation process of the MO. The sample S3 has a perfect Ag NP/ZnO NRs core/shell structure as shown in Fig. 1 and almost all the surfaces of the Ag NPs are covered with the ZnO NRs, so the photocatalytic performance of this sample is further improved. The larger specific surface area is also believed to be the main reason for the better photocatalytic performances of the sample S5 and S6 compared with the sample S3. These results indicate that the Ag nanoparticles play three main roles in improving the photocatalytic performance of the resultant samples. On the one hand, the nanocomposites with bigger specific surface area can be prepared by adding some Ag NPs colloids, which may accelerate the photocatalytic process by providing more interfaces between the MO and the catalysts. On the other hand, the formed heterostructure can inhibit the recombination of the photoinduced electrons and holes due to the addition of Ag nanoparticles, which can improve the photocatalytic performance greatly. Actually, these two factors contribute to the photocatalytic activities of the samples in our experiment together.
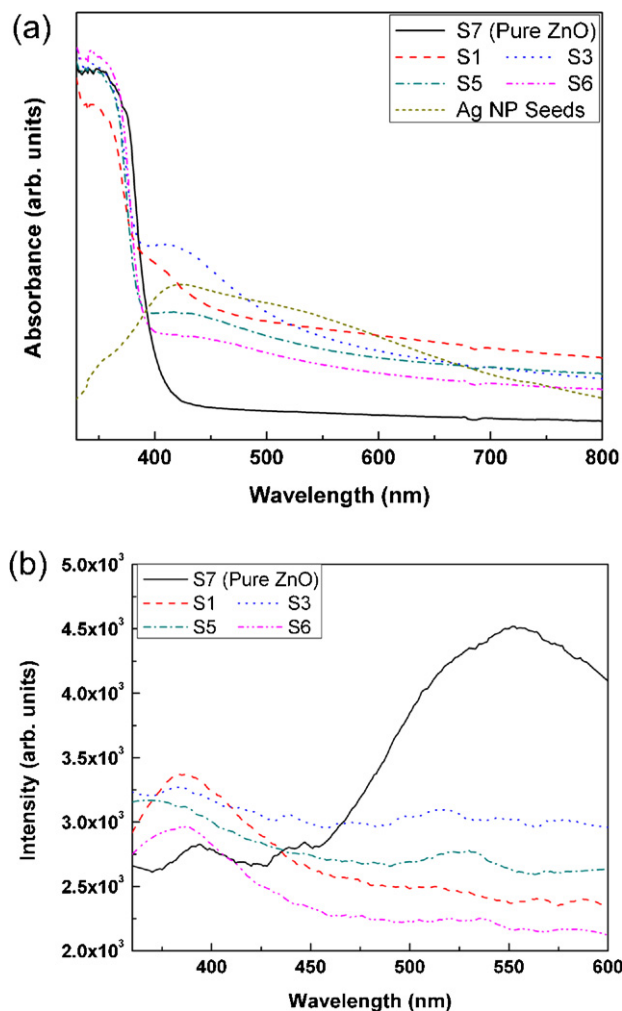
4. Conclusions

Ag NP/ZnO NRs nanocomposites with a core/shell structure have been successfully prepared by the seed-mediated method, which

is a simple and effective way to prepare hedgehog-like nanocomposites with a Ag NP in the center and ZnO NRs on the surface of Ag NPs. Results show that ZnO NRs can grow directly on the surface of Ag NPs without any other ancillary seed-assisted process and the volume content ratio of the Ag NPs colloids and the ZnO precursor solution in the reaction solution is crucial to morphological properties of the resulted nanocomposites. Well-constructed hedgehog-like Ag NP/ZnO NRs core/shell nanocomposites with a good crystalline property can be easily obtained by optimizing the volume content ratio of the Ag NPs colloids and the ZnO precursor solution of the Ag NPs and the Zn source in the overgrowth process of the ZnO NRs. Base on the above results, a possible formation process of the Ag NP/ZnO NRs has been proposed and discussed. In addition, the photocatalytic activities of some resulting samples demonstrate that the Ag NP/ZnO NRs nanocomposites have a better performance than the pure ZnO due to their larger specific surface area and the formed heterostructure.

Acknowledgements

References

[1] C.W. Zou, Y.F. Rao, A. Alyamani, W. Chu, M.J. Chen, D.A. Patterson, E.A.C. Emanuelsson, W. Gao, Langmuir 26 (2010) 11615–11620.
[2] H.Y. Yang, S.F. Yu, S.P. Lau, X. Zhang, D.D. Sun, G. Jun, Small 5 (2009) 2260–2264.
[3] Y. Sun, Q. Zhao, J. Gao, Y. Ye, W. Wang, R. Zhu, J. Xu, L. Chen, J. Yang, L. Dai, Z.-m. Liao, D. Yu, Nanoscale 3 (2011) 4418–4426.
[4] C. Xu, L. Cao, G. Su, W. Liu, H. Liu, Y. Yu, X. Qu, J. Hazard. Mater. 176 (2010) 807–813.
[5] V. Subramanian, E.E. Wolf, P.V. Kamat, J. Am. Chem. Soc. 126 (2004) 4943–4950.
[6] G. Merga, L.C. Cass, D.M. Chipman, D. Meisel, J. Am. Chem. Soc. 130 (2008) 7067–7076.
[7] J.-s. Choi, Y.-w. Jun, S.-I. Yeon, H.C. Kim, J.-S. Shin, J. Cheon, J. Am. Chem. Soc. 128 (2006) 15982–15983.
[8] K. Sun, Y. Jing, N. Park, C. Li, Y. Bando, D. Wang, J. Am. Chem. Soc. 132 (2010) 15465–15467.
[9] X.Z. Li, Y.Q. Wang, J. Alloys Compd. 509 (2011) 5765–5768.
[10] R.K. Sahu, K. Ganguly, T. Mishra, M. Mishra, R.S. Ningthoujam, S.K. Roy, L.C. Pathak, J. Colloid Interface Sci. 366 (2012) 8–15.
[11] X. Fu, J. Liu, H. Yang, J. Sun, X. Li, X. Zhang, Y. Jia, Mater. Chem. Phys. 130 (2011) 334–339.
[12] T.J. Whang, M.T. Hsieh, H.H. Chen, Appl. Surf. Sci. 258 (2012) 2796–2801.
[13] A. Pandikumar, R. Ramaraj, J. Hazard. Mater. 203–204 (2012) 244–250.
[14] Y.C. Liang, C.C. Wang, C.C. Kei, Y.C. Hsueh, W.H. Cho, T.P. Perng, J. Phys. Chem. C 115 (2011) 9498–9502.
[15] J. Wang, X.M. Fan, K. Tian, Z.W. Zhou, Y. Wang, Appl. Surf. Sci. 257 (2011) 7763–7770.
[16] Y.H. Zheng, L.R. Zheng, Y.Y. Zhan, X.Y. Lin, Q. Zheng, K.M. Wei, Inorg. Chem. 46 (2007) 6980–6986.
[17] D.D. Lin, H. Wu, R. Zhang, W. Pan, Chem. Mater. 21 (2009) 3479–3484.
[18] J.W. Chiou, S.C. Ray, H.M. Tsai, C.W. Pao, F.Z. Chien, W.F. Pong, C.H. Tseng, J.J. Wu, M.H. Tsai, C.H. Chen, H.J. Lin, J.F. Lee, J.H. Guo, J. Phys. Chem. C 115 (2011) 2650–2655.
[19] Z.J. Li, S.Y. Sun, X. Xu, B. Zheng, A. Meng, Catal. Commun. 12 (2011) 890–894.
[20] Y.T. Yin, W.X. Que, C.H. Kam, J. Sol–Gel Sci. Technol. 53 (2010) 605–612.
[21] Y. Sun, G.M. Fuge, N.A. Fox, D.J. Riley, M.N.R. Ashfold, Adv. Mater. 17 (2005) 2477–2481.
[22] C.Y. Jiang, X.W. Sun, G.Q. Lo, D.L. Kwong, J.X. Wang, Appl. Phys. Lett. 90 (2007) 263501.
[23] J. Elias, R. Tena-Zaera, G.Y. Wang, C. Levy-Clement, Chem. Mater. 20 (2008) 6633–6637.
[24] Z.C. Wang, G. Chumanov, Adv. Mater. 15 (2003) 1285–1289.
[25] S. Deng, H.M. Fan, X. Zhang, K.P. Loh, C.L. Cheng, C.H. Sow, Y.L. Foo, Nanotechnology 20 (2009) 175705.
[26] G.Y. Shan, S.J. Zheng, S.P. Cheng, Y.W. Chen, Y.C. Liu, Colloids Surf. B (2010), doi:10.1016/j.colsurfb.2012.01.037.
[27] D.H. Zhang, X.H. Liu, X. Wang, J. Alloys Compd. 509 (2011) 4972–4977.
[28] H.B. Hu, Z.H. Wang, S.F. Wang, F.W. Zhang, S.P. Zhao, S.Y. Zhu, J. Alloys Compd. 509 (2010) 2016–2020.
[29] X.T. Yin, W.X. Que, F.Y. Shen, Thin Solid Films 520 (2011) 186–192.
[30] F. Li, Y.L. Yuan, J.Y. Luo, Q.H. Qin, J.F. Wu, Z. Li, X.T. Huang, Appl. Surf. Sci. 256 (2010) 6076–6082.
[31] C.X. Song, Y.S. Lin, D.B. Wang, Z.S. Hu, Mater. Lett. 64 (2010) 1595–1597.
[32] M.E. Aguirre, H.B. Rodríguez, E.S. Rom, A. Feldhoff, M.A. Grela, J. Phys. Chem. C 115 (2011) 24967–24974.
[33] B. Wiley, Y.G. Sun, Y.N. Xia, Langmuir 21 (2005) 8077–8080.
[34] F.R. Fan, Y. Ding, D.Y. Liu, Z.Q. Tian, Z.L. Wang, J. Am. Chem. Soc. 131 (2009) 12036–12037.